ADVANCED INTELLIGENT SYSTEMS
Open Access
www.advintellsyst.com

Shape-Controlled Flexible Microelectronics Facilitated by Integrated Sensors and Conductive Polymer Actuators

Boris Rivkin, Christian Becker, Farzin Akbar, Rachappa Ravishankar, Dmitriy D. Karnaushenko, Ronald Naumann, Alaleh Mirhajivarzaneh, Mariana Medina-Sánchez, Daniil Karnaushenko,* and Oliver G. Schmidt**

The next generation of biomedical tools requires reshapeable electronics to closely interface with biological tissues. This will offer unique mechanical properties and the ability to conform to irregular geometries while being robust and lightweight. Such devices can be achieved with soft materials and thin-film structures that are able to reshape on demand. However, reshaping at the submillimeter scale remains a challenging task. Herein, shape-controlled microscale devices are demonstrated that integrate electronic sensors and electroactive polymer actuators. The fast and biocompatible actuators are capable of actively reshaping the device into flat or curved geometries. The curvature and position of the devices are monitored with strain or magnetic sensors. The sensor signals are used in a closed feedback loop to control the actuators. The devices are wafer-scale microfabricated resulting in multiple functional units capable of grasping, holding, and releasing biological tissues, as demonstrated with a neuronal bundle.

1. Introduction

Flexible electronics has gained tremendous attention over the past decades, revolutionizing fields such as telecommunication, multimedia, and healthcare.[1] Major electronic components, e.g., interconnects, antennas, diodes, and transistors, have been fabricated on thin polymeric foils to generate new options in the toolkit of developers. Applying thin polymeric foils as substrates facilitates the production of electronic systems with low weight, shape compliance, robustness, and reliability with ever-increasing complexity. The ultrathin design of these electronic devices has promoted bioelectronics that include artificial skins,[2] sensor arrays,[3] electronic implants such as brain probes,[4] and nerve cuffs,[5] to name a few. The ability to naturally conform to complex 3D shaped anatomies is a vital feature for electronic devices to interact with soft biological tissue. And while the shape of a large-area flexible electronic device can be easily adapted manually to the geometric requirements of the final application, handling becomes increasingly more challenging when aiming at smaller dimensions, when, e.g., a submillimeter nerve fiber bundle has to be enclosed gently with a similarly small cuff implant.[6] Shapeable microelectronic devices, which transform their shape on demand, provide an alternative strategy to accomplish this challenging task.[7] For instance, soft microscale structures with integrated electronic circuits have recently been demonstrated to wrap around peripheral nerves in situ when exposed to elevated temperatures or moisture.[8,9] These devices, however, lack the ability to reshape repeatedly and on demand in the operating environment. Such functionalities require the integration of biocompatible flexible shape and position sensors together with robust microactuators, fabricated ideally by a monolithic wafer-scale process.

Among a variety of small-scale actuators that are driven by pneumatic[10,11] and hydraulic[12] pressure, electric[13] and

---

B. Rivkin, C. Becker, F. Akbar, R. Ravishankar, Dr. D. D. Karnaushenko, A. Mirhajivarzaneh, Dr. M. Medina-Sánchez, Dr. D. Karnaushenko, Prof. O. G. Schmidt
Institute for Integrative Nanosciences
Leibniz IFW Dresden
Helmholtzstraße 20, Dresden 01069, Germany
E-mail: m.medina.sanchez@ifw-dresden.de; d.karnaushenko@ifw-dresden.de; o.schmidt@ifw-dresden.de

The ORCID identification number(s) for the author(s) of this article can be found under https://doi.org/10.1002/aisy.202000238.

© 2021 The Authors. Advanced Intelligent Systems published by Wiley-VCH GmbH. This is an open access article under the terms of the Creative Commons Attribution License, which permits use, distribution and reproduction in any medium, provided the original work is properly cited.

DOI: 10.1002/aisy.202000238

R. Naumann
Transgenic Core Facility
Max Planck Institute of Molecular Cell Biology and Genetics
Pfotenhauerstrasse 108, Dresden 01307, Germany

Prof. O. G. Schmidt
Material Systems for Nanoelectronics
Chemnitz University of Technology
Str. der Nationen 62, Chemnitz 09111, Germany

Prof. O. G. Schmidt
Nanophysics
Dresden University of Technology
Haeckelstraße 3, Dresden 01069, Germany

magnetic fields,[14–16] stimuli responsive polymers are attractive for creating a variety of shape-changing thin-film systems. Their shape or volume changes commonly rely on an external stimulus, e.g., heat,[17–19] light,[20–22] pH, or moisture,[23,24] which can hardly be controlled in the operating environment. In contrast to these materials, ionic electroactive polymer (IEAP) actuators rely on electrical potentials that trigger shape changes through the release or displacement of ions.[25–27] A prominent IEAP actuator technology, namely, ionic polymer–metal composite (IPMC) actuators, has been considered for biomedical applications, but is notoriously difficult to fabricate through microscale processes and requires relatively high and potentially harmful electrostatic bias voltages (3–5 V) during operation.[28,29] In contrast, actuators based on the conductive polymer polypyrrole (PPy) shrink or expand when electrically oxidized or reduced with comparably small bias voltages (<1 V) and are generally regarded as secure for biomedical and in vivo applications.[30,31] The performance of PPy actuators was studied under various physiologically relevant environments such as cerebral liquid,[32] cell culture medium,[33] and body fluids such as blood, plasma, and urine,[34] which confirmed the biocompatibility of this technology. Actuation of PPy is caused by the absorption or repulsion of hydrated ions, e.g., Na^+ from a surrounding electrolyte, which are abundant in biologically relevant environments. PPy is compatible with conventional wafer-scale manufacturing processes based on high-resolution photolithography and patterning technologies, and has been explored widely across many length scales, ranging from centimeter-scale artificial muscles[27] down to various microscale devices such as microvials,[35] actuator arrays capable of grabbing fibers,[36] or a micromanipulator based on a combination of multiple independent actuators and reinforcing elements that was capable of lifting and moving glass beads.[34]

The relatively facile fabrication of PPy actuators typically requires a noble metal electrode (usually Au or Pt) and an optional structural support layer of, e.g., polydimethylsiloxane (PDMS).[37] So-called “dry” actuators were also realized with polymer electrolytes[38] or in a sandwich structure with a polyvinylidene fluoride (PVDF) membrane and electrodes on both sides.[39]

However, despite these fascinating properties, the performance of IEAP actuators can vary dramatically depending on a multitude of factors, such as fabrication conditions,[40] degradation,[41] and ambient conditions.[42] The reliable operation of these actuators, similar to other actuation technologies in robotics, requires feedback control for reproducible reshaping. First attempts to enable reliable actuation relied on optical sensors which monitored the position of centimeter-scale IEAP actuators,[43] and although optimized control loops improved the positioning in a laboratory environment, bulky optical setups cannot be easily transferred to real-life applications.[39] Instead, means for direct position or shape sensing need to be integrated into actuated devices to enable fast and precise actuator control with little overhead. The idea to electrically probe soft actuators directly to determine their shape was brought forward as self-sensing or self-aware actuators.[22,44] These approaches, however, still struggle with noise and the decoupling of driving and sensing signals.[45] In an alternative approach, different components for actuation and sensing were mechanically coupled to circumvent noise and crosstalk.[29,46–48] There, either strain sensors were attached to actuators, or a part of the actuating polymer was electrically separated to serve as curvature sensor. Recently, Rohtlaid et al.[49] have demonstrated small-scale transducers made by means of batch fabrication at the millimeter scale, which can operate either as actuator or strain sensor at a time. Thus, to date only large centimeter-scale actuators have been demonstrated with feedback-driven positioning. These fabrication approaches, however, do not allow for monolithic integration with other microelectronic components, and therefore do not offer suitable strategies toward microrobotics.

In summary, considerable efforts have been taken to develop actuated microscale devices with integrated sensing capabilities to enable feedback control. Although some proposed integration strategies allowed for accurate feedback-driven positioning, these systems could only be realized at the centimeter scale. A flexible microscale device with independent actuators and sensors, which would enable feedback-driven shape control and pave the way toward soft microrobotic systems,[50,51] remains to be demonstrated to date.

Here, we present reshapeable microelectronic devices (RMEDs), useful in future biomedical applications including gentle surgical clamps and force tunable nerve cuffs, to name a few. These devices feature integrated micropatterned actuators and sensors for active reshaping with a proportional-integral-derivative (PID) controller (**Figure 1**A). The reshaping of an ultrathin polyimide (PI) carrier platform is achieved with integrated PPy-based actuators that respond to low voltage electric cues. The bias voltage required for the actuator is computed according to an electric signal generated by the integrated sensors. The feedback control compensates for varying operating conditions and improves positioning. This enables active interfacing with the environment such as controlled grasping and release of biological tissues. We demonstrate two complementary solutions for measuring the curvature of RMEDs and their position (Figure 1B). Namely, we integrate gold stripe strain gauges (GSSGs)[52] which allow to measure the device curvature directly. Furthermore, spin valve magnetic sensors (SVMSs) allow to assess the orientation[53] of the RMEDs by probing static or low-frequency magnetic fields as nonharmful reference that can fully penetrate nonmagnetic materials and biological tissues. We fabricated numerous RMEDs in a monolithic wafer-scale process, exploring shapeable polymer technologies.[7,8,24,54–56]

2. Results

2.1. Estimation of Optimal Thicknesses for RMEDs

RMEDs require free carrier surface to integrate sensors and interconnects apart from the actuators. However, in previous reports where IEAP microactuators have been coated onto flexible carriers,[37,49] the IEAP polymer and their electrical connections generally occupied all or most of the available area of the supporting film. In this work, we achieved extensive curvature control of RMEDs with two actuator stripes located along the edges of the thin-film PI support, occupying as little as 20% of the total available area. The remaining 80% of the area is used for other electronic functionalities. To achieve high actuation

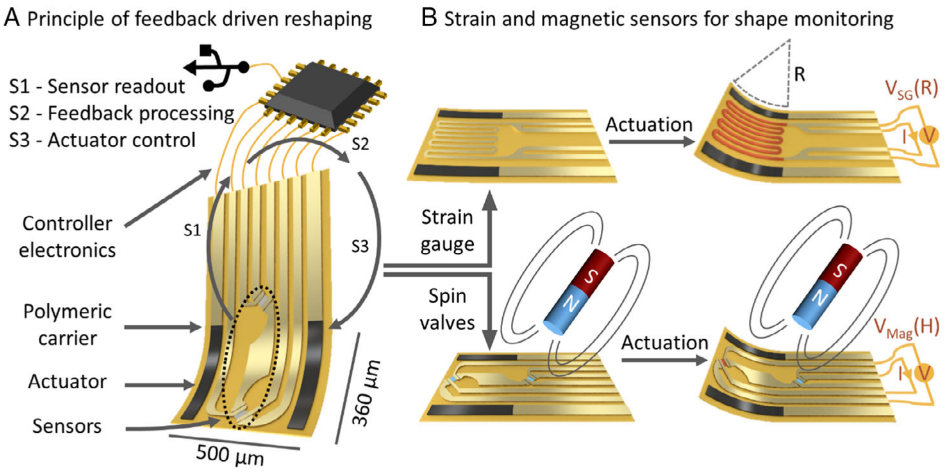
A Principle of feedback driven reshaping
S1 - Sensor readout
S2 - Feedback processing
S3 - Actuator control
Controller electronics
Polymeric carrier
Actuator
Sensors
S1
S2
S3
360 µm
500 µm
B Strain and magnetic sensors for shape monitoring
Actuation
R
$V_{SG}(R)$
I
V
Strain gauge
Spin valves
S
N
Actuation
$V_{Mag}(H)$
I
V

Figure 1. Concept of the reshapeable microelectronic devices. A) Artistic illustration. A thin polymer film carries sensors that assess the device shape (S1). An external controller processes the sensor data (S2) and applies a bias voltage to a pair of PPy actuators to reshape the device (S3). B) Two different approaches to monitor the device shape. Top: A strain gauge directly measures the curvature. Bottom: Magnetic sensors assess the deflection by probing a reference magnetic field.

performance with only fractional actuator coverage, it is crucial to determine the optimal thicknesses of the PI support, Au electrodes, and the PPy layer.

The actuator strain is determined by the redox-induced influx or repulsion of hydrated ions such as sodium. The resulting curvature κ of the RMED is associated with a bending radius $R = \kappa^{-1}$ (**Figure 2**A). The maximum curvature that any carrier/electrode/PPy stack can achieve is a product of the actuator strain α and the device's curvature coefficient c_κ, therefore $\kappa = \alpha \cdot c_\kappa$. The latter depends on the stiffness of the individual layers and their relative and absolute thicknesses.

Christophersen et al.[57] developed a comprehensive mechanical model of curving Au/PPy actuator bilayers and provided experimental verification. A key finding was that the highest

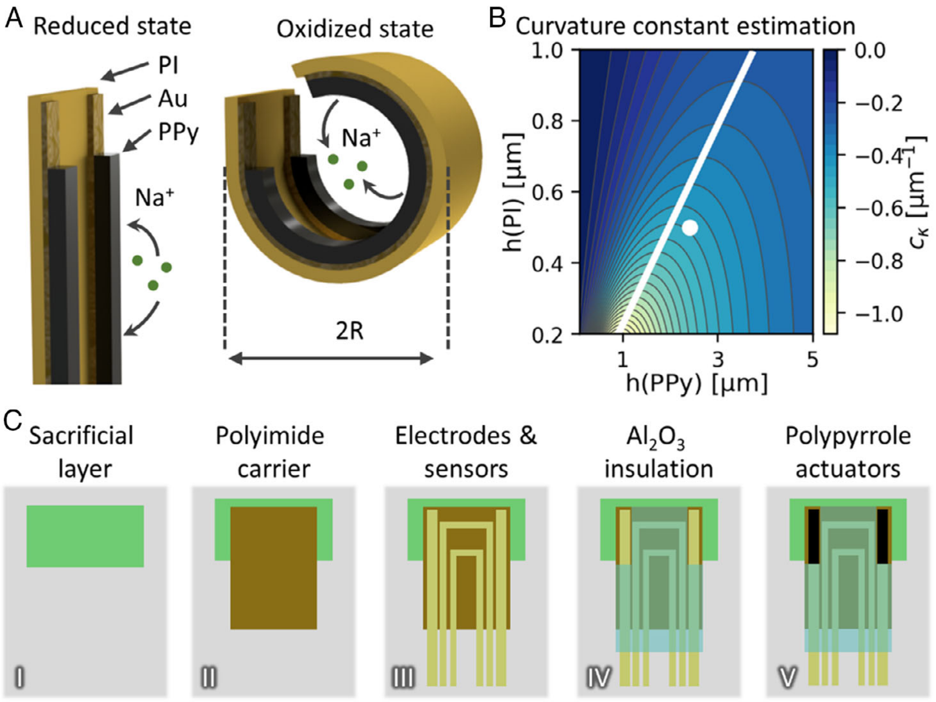
A Reduced state
Oxidized state
PI
Au
PPy
Na^+
Na^+
2R
B Curvature constant estimation
1.0
0.8
0.6
0.4
0.2
h(PI) [µm]
1
3
5
h(PPy) [µm]
0.0
−0.2
−0.4
−0.6
−0.8
−1.0
c_κ [µm^{-1}]
C Sacrificial layer
Polyimide carrier
Electrodes & sensors
Al_2O_3 insulation
Polypyrrole actuators
I
II
III
IV
V

Figure 2. A Theoretical optimization and fabrication of reshapeable microelectronic devices. A) The PI/Au/PPy layer stack is flat in the reduced state and gradually curls up upon oxidation. The curled shape is described with the curvature κ, which is the inverse of the curvature radius R. B) Computed curvature coefficient c_κ for RMEDs with different PPy and PI layer thicknesses. The line indicates the optimal PPy thickness for each PI thickness; the dot indicates the optimized device used in this study. C) Fabrication routine of RMEDs.

curvature is achieved with a specific thickness ratio of the passive support and the contracting PPy. Both thinner and thicker PPy films, compared with the optimum, provided less actuation for given support thickness. Based in the work of Christophersen et al. and others, Du et al.[58] developed a model that is well suited to describe devices with more than two layers, as presented in this work. The authors analyzed the bending mechanics of a multilayer stack of PI, a metal electrode, and PPy. It allows to compute the curvature coefficient c_κ of the device as a function of the various thicknesses and Young's moduli of the materials incorporated in the stack. We computed c_κ for combinations of PI and PPy thicknesses with the ranges of 0.2–1.2 μm and 0.1–5 μm, respectively. The material properties of photopatterned PI as well as Au and Al_2O_3 have been reported in available literature[8,58,59] The Young's modulus of PPy was determined by means of atomic force microscope (AFM) microindentation as literature values can vary drastically. The measurements yielded a value of 0.5 GPa, which is well within the commonly reported range. We accounted for the different areas of the components by adjusting the stiffness of PI, Al_2O_3, and Au, with the corresponding factor of 5, 3, and 3, respectively. Figure 2B shows a color-coded map that provides the curvature coefficient for each considered combination of PI and PPy thicknesses. The white line indicates the optimal PPy thickness for each PI thickness, i.e., the ratio that yields the highest curvature. Deviation from the ideal ratio, both toward thinner and thicker PPy layers, reduces actuation range as already discussed by Christophersen et al. The trace which indicates optimal thickness ratios follows a linear relationship $h_{\mathrm{PPy}} = 3.6 \cdot h_{\mathrm{PI}} + 0.2\ \mu\mathrm{m}$, which is within reasonable agreement with previous estimates. It should be noted that achievable curvatures overall decrease with increasing film thicknesses, as was also already noted in previous reports.[57] This provides the important implication that PPy actuators are most efficiently applied in thin-film and microscale devices. For this study, we have chosen the PI carrier thickness of 0.5 μm as a decent compromise between flexibility and robustness. Consequently, a PPy thickness of around 2 μm served as starting point for device optimization.

2.2. Monolithic Wafer-Scale Fabrication of RMEDs

Device fabrication is shown in Figure 2C where the preparation starts with a rectangular metal–organic sacrificial layer (SL) and a rectangular PI carrier ($350 \times 500\ \mu\mathrm{m}^2$) by means of spin coating and photolithography. The PI platform is anchored to the glass substrate from one side and its thickness was controlled by the spin coating speed. RMEDs with SVMS were fabricated through sputter deposition and lift-off patterning of ellipsoidal multilayer stacks. The fully optimized stack was previously reported[53] and is composed of $\mathrm{Ta}^{5.0\,\mathrm{nm}}/\mathrm{Ni}_{80}\mathrm{Fe}_{20}{}^{2.0\,\mathrm{nm}}/\mathrm{Co}_{90}\mathrm{Fe}_{10}{}^{0.6\,\mathrm{nm}}/\mathrm{Cu}^{1.6\,\mathrm{nm}}/\mathrm{Co}_{90}\mathrm{Fe}_{10}{}^{0.6\,\mathrm{nm}}/\mathrm{Ni}_{80}\mathrm{Fe}_{20}{}^{1.0\,\mathrm{nm}}/\mathrm{Ru}^{0.8\,\mathrm{nm}}/\mathrm{Co}_{90}\mathrm{Fe}_{10}{}^{1.0\,\mathrm{nm}}/\mathrm{Ni}_{80}\mathrm{Fe}_{20}{}^{1.0\,\mathrm{nm}}/\mathrm{Ir}_{19}\mathrm{Mn}_{81}{}^{8.0\,\mathrm{nm}}/\mathrm{Ta}^{2.0\,\mathrm{nm}}$. Next, a set of Au electrodes that serve as contacts for PPy actuators, as contacts for sensors, and as GSSGs were fabricated with a standard lift-off process and electron beam evaporation. The devices were chemically and electrically insulated with a patterned layer of Al_2O_3. Contact pads and designated actuator areas were left free from Al_2O_3. This insulating layer was deposited with an atomic layer deposition (ALD) process and etched chemically. To finalize RMEDs, the glass wafers which carry 22 RMEDs each (**Figure 3**A) were cut, and individual devices were electrically connected and immersed in a three-electrode setup for electrochemical polymerization. Exposed Au electrodes were plated with PPy following adapted procedures reported by Smela et al.[31] (details in the Experimental Section). The deposition voltage was kept constant and the total supplied electric charge served as an indicator for the PPy thickness. As the resulting PPy actuators occupy no more than 20% of the overall device area ($0.175\ \mathrm{mm}^2$), the rest of the area (80%) is available to carry either SVMSs (Figure 3B) or GSSGs (Figure 3C) in between the pair of actuator stripes. The option to integrate virtually any microscale electronic component is a unique feature among microscale IEAP actuators with flexible carriers, and hereby demonstrated for the first time with two different sensor types. The area of previously reported devices was generally mostly covered by the conductive polymer stack.[31,35,49]

Shape conformation changes require that the micropatterned actuator is partially delaminated from the wafer in a controlled way. For microscale PPy actuators, this is a challenging task which has previously been tackled by differential adhesion[31] or the selective removal of a metallic SL.[34] Both approaches leave room for improvement,[36] as the former imposes restrictions on materials choice and device layout, and the latter is generally time-consuming and requires etchants which can be harmful to the actuators. Here, the used metal–organic SL[55,56] can be selectively etched over a period of 20 min to delaminate the devices from the substrate. In short, this film consists of a lanthanum cross-linked polyacrylic acid network. The SL can withstand temperatures of at least 300 °C and is insoluble in water, developer solutions, and many organic solvents. The SL is selectively etched when the polyacrylic acid is protonated in mild acids (e.g., 2% diluted HCl) or La^{3+} is stripped out of the film by a strong chelating agent (e.g., diethylene triamine pentaacetic acid). Both reactions turn the film water soluble and overlying layers are under-etched with a typical rate of $10\ \mu\mathrm{m\ min}^{-1}$. This fast process imposes no immediate adverse effects on the actuators and is applicable to virtually any material system. Our release technology significantly facilitates the parallel and reliable release of PPy actuators from the substrate with high yield and short production time.

RMEDs were immersed into an electrolyte solution after the release to carry out actuation experiments. With small bias voltages ($<\pm 1$ V vs Ag/AgCl) the optimized device can then be set into a planar, or curled up shape with different curvatures (Figure 3C). Actuation occurs immediately after a change in bias voltage, while full curling or uncurling can be achieved within less than 0.5 s. Although the main subject of this study are RMEDs with a width of 500 μm and two actuator stripes, RMEDs with a width of 750 μm and three actuators were realized as well. Such a device can be seen in Movie S1, Supporting Information, where it is used to demonstrate reversible, gradual, and rapid reshaping following a user input. The actuators operate with very small currents, typically less than 10 μA (Figure 3D), far below the safe level for humans of 1 mA,[60] and require only 1.6 μJ of electrical energy to fully reshape the RMED. Our actuators can withstand more than 1000 actuation cycles without significant degradation at an actuation frequency of 0.05 Hz over

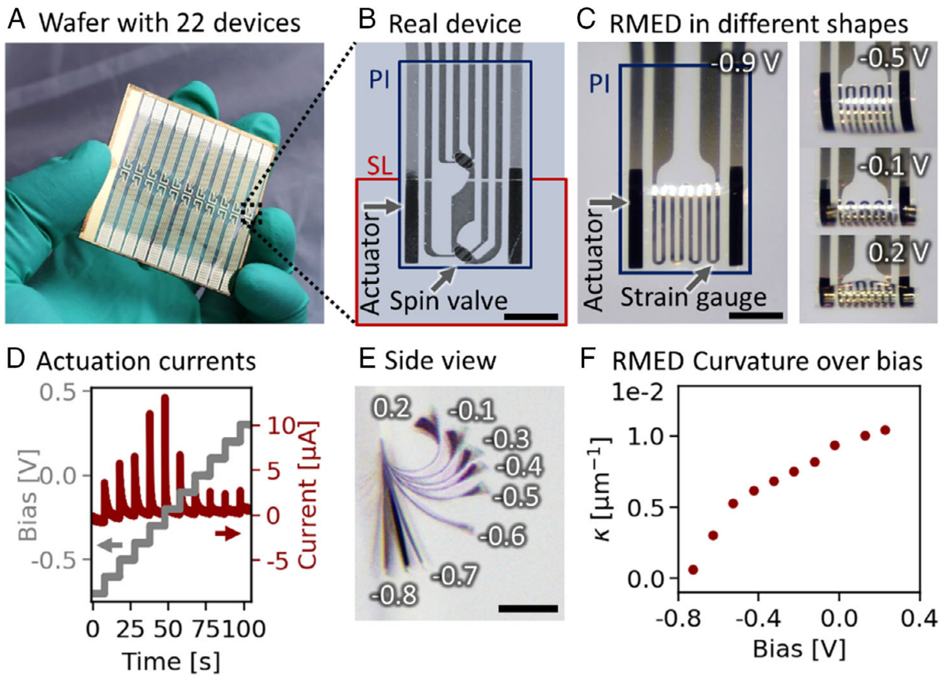

Figure 3. Real RMEDs as fabricated on $50 \times 50\,\text{mm}^2$ glass substrates and actuator characterization. The size of all scale bars is 200 µm. A) $50 \times 50\,\text{mm}^2$ glass substrates with 22 RMEDs. B) Micrograph of RMED with actuators and SVMSs before release from the substrate. C) RMED with a strain gauge after release in various curvature states. D) Voltage and current curves of stepwise actuation of a RMED. E) Side view overlay of an RMED with various bias voltages (indicated in Volt) allow to measure the device curvature of up to $(90\,\mu\text{m})^{-1}$. F) Graph of RMED curvatures derived from side view micrographs in dependence of the applied bias voltage (vs Ag/AgCl).

a time period of 5 h (see Figure S1, Supporting Information). We have chosen conservative testing conditions with the rate corresponding to a scan rate of $100\,\text{mV}\,\text{s}^{-1}$, commonly applied when characterizing conductive polymer (CP) actuators. The actuation rate of $\approx 18^\circ\text{s}^{-1}$ is appropriate for this type of device to accomplish grabbing and manipulation tasks. We have not observed any delamination of the actuator or sensor metal electrodes from the PI, neither during this stability study, nor during any other experiments conducted with the RMEDs. We attribute this stability to the small estimated strain at the Pi/Ti/Au interface ($\approx$0.15%) and the strong adhesion between Ti/Au and PI carrier. Fabrication details can be found in the Experimental Section. The blocking force of the actuated device was estimated by balancing a sample weight in such a way on the device that the gravitational force of the weight was countered only by the RMED. The resulting force of the RMED was around 3 mN (corrected for buoyancy) and the RMED was able to lift this load over a vertical distance of 50 µm (see Figure S2, Supporting Information). A similar study has been conducted by Smela et al.,[61] where 70 microactuators ($30 \times 100\,\mu\text{m}^2$) were able to bend while lifting a sample weight of 3.3 mg. When the sample weights are corrected for buoyancy and the actuator areas involved, the lifting performance strongly resembles the results obtained in this study (Smela et al. $\approx 9.1\,\text{N}\,\text{cm}^{-2}$ vs $\approx 8.3\,\text{N}\,\text{cm}^{-2}$ here).

Figure 3E shows a micrograph overlay of multiple steady states of one RMED with the corresponding bias voltages, where the actuation was observed from the side. This perspective allows to estimate the curvature of the device. The RMED is completely flat at −0.8 V versus Ag/AgCl. The highest curvature of approximately $\kappa = (90\,\mu\text{m})^{-1} \approx 0.01\,\mu\text{m}^{-1}$ is reached at 0.2 V, which is similar to previously reported curvatures for bilayer actuators with relatively thick support layers, but smaller compared with devices with thin support layers.[57] The experimental optimization of the layer stack was based on the computation of the optimal thickness ratio (Figure 2B). Here, a series of devices with a PI thickness of 0.5 µm and PPy thicknesses of 1.2, 1.7, 2.0, 2.4, 3, and 3.7 µm were fabricated. Only devices with a PPy thickness of 2 and 2.4 µm achieved the highest curvature of $0.01\,\mu\text{m}^{-1}$, thus forming three quarters of a circle, in agreement with the previously calculated estimates. Both thinner and thicker PPy layers resulted in smaller curvatures, shaping the device to only a quarter circle. The achieved curvature is relevant for devices serving as, e.g., microscale nerve cuffs or nerve clamps. Figure 3F shows the device curvature in dependence on the bias voltage. The highest rate of actuation is observed when reshaping from the flat device state (−0.8 V) toward intermediate curvatures. Above −0.5 V, the curvature increases slower with increasing bias voltage until it saturates above 0.1 V. However, it should be noted that this bias-curvature map is not universally accurate, as the actuation amplitude is largely affected by fabrication and operation conditions. A general and more reliable approach requires feedback to monitor the shape of the device, which we address by developing two different strategies.

2.3. Monitoring and Controlling the RMED Position with Integrated Magnetic Sensors

Magnetic fields are widely applied in position and orientation sensing. In the biomedical field, static and low-frequency magnetic fields are successfully used for tasks such as catheter position tracking with ultralow fields of 5–50 μT[62] and steering.[63] Low-frequency magnetic fields (≈12 mT for frequencies <1.6 Hz), in contrast to high-frequency ones, do not interact with biological tissues and therefore do not suffer from electromagnetic shielding and are less critical from the perspective of electromagnetic safety.[64]

In this study, the shape of RMEDs is monitored with integrated magnetic sensors which probe an external reference field, as shown in **Figure** 4A. The elliptically shaped sensor stacks ($85 \times 55\ \mu m^2$) are positioned pairwise, one anchored to the substrate (sensor 1) and the second at the tip of the free-standing polymeric carrier (sensor 2). These sensors operate as follows: the magnetization of the "free layer" is aligned with the magnetization of an external magnetic field, while the magnetization direction of a "reference layer" (Figure 4A) is permanently magnetized during the device fabrication when the magnetic stacks are annealed in a magnetic field.[53] The electrical resistance of the entire stack depends on the relative orientations of the magnetization directions of the reference and free layers. The resistance is lowest when the magnetization directions are parallel, and highest when the magnetization directions are antiparallel. Upon actuation, sensor 2 is deflected relative to sensor 1 by an angle θ (Figure 4A), where $\theta = 0°$ corresponds to the flat and $\theta = 180°$ corresponds to a U-shaped state. The latter case is relevant for grabbing objects or clamps. When $\theta > 0$, an external magnetic field results in different orientations

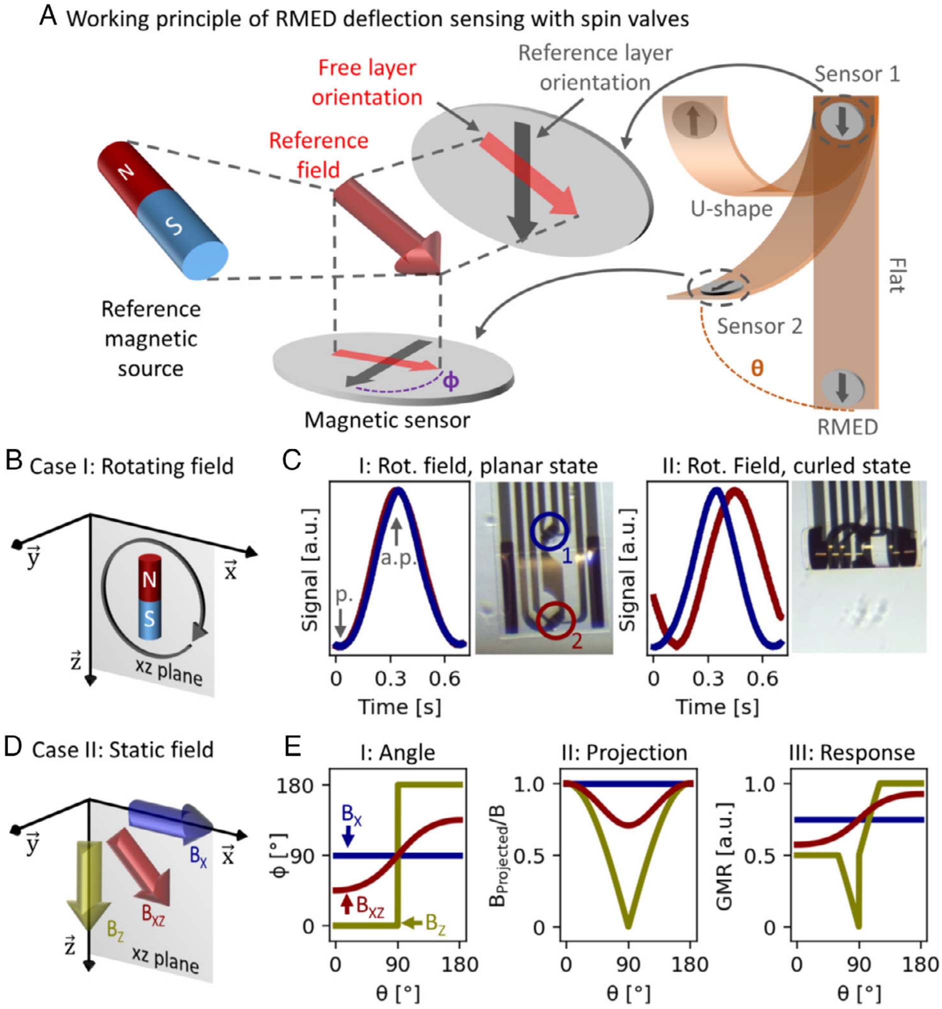
A Working principle of RMED deflection sensing with spin valves
Free layer orientation
Reference layer orientation
Reference field
Sensor 1
N
S
Reference magnetic source
U-shape
Flat
Sensor 2
θ
ϕ
Magnetic sensor
RMED
B Case I: Rotating field
y⃗
x⃗
z⃗
N
S
xz plane
C
I: Rot. field, planar state
II: Rot. Field, curled state
Signal [a.u.]
a.p.
p.
1
2
0 0.3 0.6
Time [s]
D Case II: Static field
B_X
B_XZ
B_Z
xz plane
E
I: Angle
II: Projection
III: Response
ϕ [°]
180
90
0
B_X
B_XZ
B_Z
B_Projected/B
1.0
0.5
GMR [a.u.]
0 90 180
θ [°]

Figure 4. Working principle and characterization of reshapeable microelectronic devices with magnetic sensors. A) Definition of the sensor deflection angle θ and the angle between reference and free layer orientations ϕ upon deflection from a flat to a U-shaped state. B) First possible configuration of the reference magnetic field: rotating in the XZ plane. C) Normalized signal of two sensors carried by the same RMED. The signals are in phase in the planar (I), and out of phase in the curled up (II) state. D) Second possible configuration of the reference magnetic field: static fields along either the X axis (B_X), the Z axis (B_Z), or tilted in the XZ plane by 45° (B_{XZ}). E) Computational estimation of key parameters of the projected field upon actuation: (I) sensor angle ϕ, (II) relative strength of the projected field, and (III) the resulting GMR sensor signal. The computations considers different orientations of the magnetic field $B = B_X$, $B = B_Z$, and $B = B_{XZ}$.

of the free layer magnetization of sensors 1 and 2, which align along the field projections on the sensor planes. The angle ϕ between a sensor's free and reference layer is measured electrically to determine the device orientation with respect to the orientation of the external magnetic field.

The external magnetic field can either rotate in one plane (Figure 4B) or be static. A permanent NdFeB magnet mounted on the rotor of an electromotor provides the required magnetic field. In the first configuration (case I), the initially flat RMED with magnetic sensors is characterized under an external rotating magnetic field (10 mT at 90 rpm) to demonstrate the basic functionality of the device. The field vector rotates in a plane parallel to the surface of the RMED. The electric responses are synchronous and show a characteristic sinusoidal shape for both sensors, in this way demonstrating that the external rotating magnetic field is perceived identically by both sensors when the carrier is flat (Figure 4C-I). The particular characteristics in the flat state allow us to derive key metrics of the sensors. For instance, when the reference and free layers are oriented in parallel, the resistances of sensor 1 and 2 are 16.02 and 16.86 Ω, respectively. When the layers are oriented antiparallel, the resistances of sensor 1 and sensor 2 are 16.62 and 17.53 Ω, respectively. This peak-to-peak difference determines the dynamic range of the sensors (≈5%), and the signal-to-noise ratio (SNR ≈ 100), which is comparable with previously reported results.[53]

For this experiment, the SVMSs were magnetized with a 45° tilt relative to the actuation axis. This configuration is advantageous for measurements in rotating fields because it prevents phase ambiguities.[53] In the actuated state, where the sensors face each other (Figure 4C-II), the response of sensor 2 preserves the characteristic sinusoidal shape, thereby confirming that CP actuators and magnetic sensors can be operated on the same polymer carrier without undesired interference. Although the curvature of the carrier could potentially affect the sensor performance due to a stress or strain caused magnetomechanical effect, the ultrathin layer stack limits the strain at the sensor plane to less than 0.15% and prevents such advert effects, as was already found for this sensor type on similarly curved surfaces.[53] The phase offset of sensor 2 with respect to the reference sensor 1 results from the different sensor plane projections of the reference field onto the two sensor planes, which is the basis of orientation encoding using SVMS.

A static magnetic field is sufficient to assess the device deflection. However, such a field needs a specific alignment to enable meaningful measurements with SVMSs. We estimated the response of the sensors under various static magnetic fields computationally to identify a suitable reference field orientation. In the static field case, the correct sensor operation requires two conditions to be met: the strength of the in-plane projection ($B_{\text{Projected}}$) of the magnetic field should be sufficiently strong (5–50 mT)[53] to align the free layer along the field direction, and the sensor response should be monotonous and unambiguous with respect to the deflection angle θ. To find a suitable field configuration that fulfills these requirements, we calculated the dependence of angle ϕ between reference and free layer orientation, $B_{\text{Projected}}$, and the giant magnetoresistance (GMR) sensor response for three different field orientations. We assumed external fields that either align along the X axis (B_x, blue), the Z axis (B_z, green), or is tilted by 45° in between the X and Z axis (B_{xz}, red), as shown in Figure 4D. The sensors' reference layer magnetizations were always oriented along the Z axis in the flat device state at $\theta = 0°$ as this magnetization allows for the higher dynamic range with a static reference field. To estimate the response to deflection, we assumed an idealized sensor response (in a.u.) to field strength given as

$$\text{GMR}_B(B) = \begin{cases} 0.05\,\text{mT}^{-1} \cdot B & \text{for } B < 10\,\text{mT} \\ 0.5 & \text{for } B \geq 10\,\text{mT} \end{cases} \tag{1}$$

An ideal sinusoidal response, with minimal resistance for parallel free and reference layers, and maximal resistance for anti-parallel orientation, is expected and can be described as $\text{GMR}_\phi(\phi) = 0.25 \cdot (1 - \cos(\phi))$. The resulting total GMR is the sum $\text{GMR} = \text{GMR}_B + \text{GMR}_\phi$.

We calculated the parameters of the field projected onto the sensor plane upon a sensor deflection angle θ, ranging between 0° and 180°. In the configuration B_x, the field projection is invariable (Figure 4E-I,II) for both ϕ and $B_{\text{Projected}}$ for any given deflection of the sensor 2. Because the estimated sensor response is a flat line (Figure 4E-III, blue), this configuration was not suitable for deflection feedback. Applying the field B_z, the angle ϕ was constant, apart from one step at $\theta = 90°$ (Figure 4E-I, green), and $B_{\text{Projected}}$ dropped to 0 mT at $\theta = 90°$ (Figure 4E-II, green) when the external field and the sensor plane were orthogonal. The estimated GMR was partially flat with respect to θ, and an ambiguity arose for angles around 90° as one GMR value could result from different deflection angles θ. Similar to the first configuration, the second one has a disadvantageous symmetry with respect to the deflection axis and is therefore not suitable. The third configuration B_{xz} breaks this symmetry and results in a gradual and monotonous variation of ϕ from 45° to 135° upon deflection of the SVMS (Figure 2E-I, red). The in-plane field projection was consistently high, e.g., at least 7 mT for a 10 mT external field (Figure 4E-II, red), and sufficient to align the free layer of the SVMS. This configuration provides an unambiguous map between ϕ and an actuation angle $0° < \theta < 180°$ (Figure 4E-III, red), allowing for position control of the RMED. The incorporation of magnetic sensors adds another layer of complexity to actuated microscale devices. As microactuators will in future enable complex microrobotic systems with a multitude of components and many degrees-of-freedom, this higher level of device complexity will be an absolute necessity to provide comprehensive feedback.

We implemented a software PID control loop[65] to drive the actuator with a bias voltage in real time. The control function was defined as $\Delta\text{Bias}_i = K_\text{P} \cdot e_i + K_\text{I} \cdot e_i \cdot \text{d}t + K_\text{D} \cdot (e_i - e_{i-1}) \cdot \text{d}t^{-1}$, where i is the control step, $\text{d}t = 0.02$ s is the constant time interval between successive steps, $e_i = P - S_i$ is the error function derived from the sensor feedback signal S_i and the desired setpoint P, and three parameters, namely, K_P—proportional, K_I—integral, and K_D—differential gain constants. The RMED was connected to a custom developed printed circuit board (PCB) with integrated analog-to-digital converters (ADCs) and digital-to-analog converters (DACs) for actuator and sensor operation (**Figure 5**A). The setpoint, feedback, and output (actuator bias) curves of a typical operation are shown in Figure 5B for $K_\text{P} = 200$, $K_\text{I} = 0$, and $K_\text{D} = 0$. When the setpoint is changed (gray step function in Figure 5B), a discrepancy (error) arises

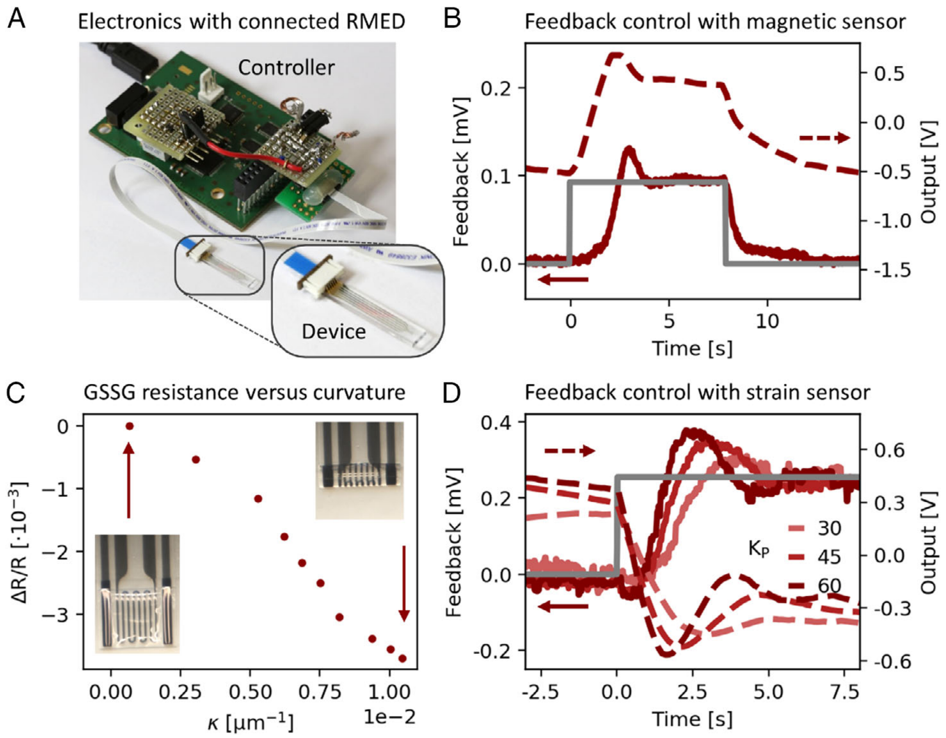

Figure 5. Operation of reshapeable microelectronic devices with strain or magnetic sensors in closed feedback loops. A) Custom-developed electronics for experimental control and device interfacing. B) Setpoint, feedback, and output curves of a typical feedback-driven positioning experiment. Position feedback was provided by integrated magnetic sensors. The proportional gain constant was set to $K_P = 200$. C) Strain sensor signal directly reflects the curvature of an RMED. Curvature estimated from side view micrographs in Figure 3E. D) Proportional feedback controller reshapes an RMED with various proportional gain parameters K_P when the setpoint is changed.

between the setpoint and the feedback signal. This causes the control loop to adjust the bias voltage to reshape the RMED, which, in turn, brings the sensor to its new position until the feedback (sensor signal) reaches the setpoint. The bias voltage increases from −0.5 to 0.7 V over a period of 2.2 s. The RMED shape changes, as monitored with the magnetic sensor, slowly at first, and at a much higher rate once the bias voltage reaches 0.5 V. It should be noted that these actuator biases were applied in a two-electrode setup without a reference, and therefore are offset to higher voltages when compared with those in Figure 3. The RMED feedback reaches the setpoint for the first time after 2.6 s and a 40% overshoot is observed before the system equilibrates around the new setpoint after another 0.8 s, yielding a total of 3.4 s for this reshaping task. A demonstration of a real-time feedback-driven positioning with user interface input is provided in Movie S3, Supporting Information.

The performance of presented systems is strongly impeded by the PID controller, both with regard to accuracy (overshoot) and speed. Compared with the seemingly instantaneous reshaping trigger by a sudden change in voltage (e.g., as shown in Movie S1, Supporting Information), the feedback-controlled reshaping requires more than 3 s. The reason is the software PID controller, which is readily implemented for demonstration purpose, but has only limited applicability. The time required for the ramp up is predefined by the control parameters since $K_P = 200$ and $\mathrm{d}t = 0.02$, the bias change rate is less than $\Delta U/\Delta t < 200 \cdot 0.1\,\mathrm{mV} \cdot (0.02\,\mathrm{s})^{-1} = 1\,\mathrm{V\,s^{-1}}$ with an maximum error (= setpoint − feedback) of 0.1 mV. A faster increase in the bias voltage could be achieved with higher proportional gain K_P or the introduction of a nonzero integral gain K_I, which, in turn, leads to higher overshoot or oscillations, as shown in Movie S3, Supporting Information. The performance of the presented system can be drastically improved through the implementation of a specialized control algorithm. This, however, is beyond the scope of this study, which primarily focuses at the development of the reshapeable sensor–actuator device. Other works have studied the feedback control of macroscopic IEAP actuators extensively, showing that dedicated algorithms decisively outperform a common PID controller,[66] e.g., by reducing the rise time by 18 times.[43] The implementation of an optimized control algorithm will be subject to future studies.

2.4. Monitoring and Controlling the RMED Shape with Integrated Strain Gauge Sensors

Shape assessment based on an external magnetic field can be applied for positioning in absolute space. For grabbing or manipulating soft tissues, however, the direct assessment of the real curvature of the RMED is crucial. In this work, the curvature of RMEDs was directly measured by acquiring the signal from the integrated GSSG. GSSGs were formed from a gold meander with a width of 15 µm and a total length of 1.2 mm. This particular strain sensor was selected because it provides a simple, yet reliable feedback source for the device curvature. The Au-based strain gauge integrates naturally into the thin-film architecture of the RMEDs and is simultaneously fabricated in a single step together with electrodes for the PPy actuators. Upon curling, the surface of the PI platform that carries actuators and sensors experiences compressive strain, which, in turn, compresses the strain gauge electrode and reduces its ohmic resistance. The resistance was measured in a pseudo four-point configuration with a biasing current of 1 mA. A movie highlighting the device operation with simultaneous RMED micrograph and sensor signal can be found in Movie S2, Supporting Information. Figure 5C shows the dependence of the GSSG resistance on the RMED curvature. The curvature values were taken from the measurement shown in Figure 3F and the sensor signal was collected and averaged over a period of 4 s. The highest resistance of $270\,\Omega$ occurs in the flat state and monotonously decreases for higher curvatures by a relative portion $\Delta R/R \approx 0.37\%$. As the basis of this measurement is ohmic resistance, it is susceptible to temperature variations and requires referencing with a temperature sensor. We estimated the temperature dependence of the sensor to be $0.45\,\Omega\,\mathrm{K}^{-1}$ from temperature-resistance measurements, as shown in Figure S3, Supporting Information. The SNR of approximately SNR ≈ 12 allows to distinguish about as many distinct shapes.

The monotonous strain sensor signal allows a direct measurement of the device curvature and is therefore readily implemented as the feedback source in a simple PID controller, comparable with the SVMSs discussed previously. Feedback control is essential for any type of robotic system. Although it was demonstrated that the performance of CP actuators can be significantly improved by model-driven control schemes such as feedforward control,[39] feedback control is required to operate actuated devices in a dynamic environment, e.g., when the presence or location of obstacles is unknown. We applied PID control to tune the RMED curvature using the GSSG signal with the proportional gain K_P either 30, 45, or 60 (Figure 5D), while K_I and K_D were set to zero. When the setpoint is changed by the operator, the controller gradually adjusts the output, i.e., the actuator bias voltage, at a rate that depends on the proportional gain parameter. The setpoint was reached for the first time after 2–3 s for all controller configurations, similar to the control experiment with the SVMS. After an overshoot and stabilization time, accurate positioning was achieved in less than 6 s in all cases. Oscillations which are typical of poorly tuned PID controller were clearly observed for the most detuned configuration with $K_P = 60$. As with the previously discussed SVMS-based feedback control, the positioning performance is limited by the controller. Here, the algorithm requires 1.5–3 s to ramp up the bias voltage according to the chosen parameters and, at the same time, overestimates the required voltage level, thereby limiting the actuation speed and precision. The rise and settling time can be drastically reduced with an optimized control algorithm, as reported in available literature.[43]

We studied the behavior of the RMED under mechanical payload to mimic an application case by placing hard and soft objects in the actuation path and thereby restraining the reshaping process (**Figure 6**A). The response of the GSSG sensor is shown in Figure 6B for the different cases. During free actuation, the sensor signal monotonously decreases while the bias voltage is increased and the RMED curls up. Then, we used a microtiter pipette as a hard obstacle, which completely inhibits curling of the RMED after contact. The strain sensor signal initially follows the reference curve, but remains constant after touching the obstacle. In contrast to a hard obstacle, a soft obstacle, such as the mouse sciatic nerve fiber used for this study, has very low stiffness. During actuation against this soft obstacle, the strain sensor reveals that the curvature further increases after contact, although to a lesser extent when compared to the unloaded reference curve. In this case, the RMED is able to compress the gel-like tissue to some degree. This insight is critical with regard to applications of RMEDs as tools for neural surgery, as nerve fibers should be approached cautiously to avoid tissue damage. Feedback controlled micromanipulators offer the possibility to eliminate human error when manipulating soft tissues that cannot withstand high pressure. During operation, such a manipulator should first detect the object and then apply a predefined force.

For this purpose, we implemented an obstacle detection algorithm in the PID control loop. First, a device was fully reshaped without mechanical load and the sensor response versus bias voltage was recorded for calibration purposes as in the "free actuation" case in Figure 6B. Then, an obstacle was placed in front of the RMED and a feedback-driven positioning experiment was conducted. During actuation, the sensor signal was compared with the expected sensor signal according to the calibration. The controlling software flagged an obstacle detection when a deviation of 20% between expected and measured signal occurred. At this instant, the controller would hold the actuation bias voltage, effectively keeping the actuator in a constant position.

When feedback-controlled actuation was performed against a hard obstacle, the feedback curves could not approach the setpoint (Figure 6C) because the required curling was prohibited. Without the obstacle detection algorithm, the bias rose to the maximum allowed voltage of 0.4 V, which led to an undesired off-axis deformation of the RMED (Figure 6D-I). In contrast, with activated obstacle detection algorithm, the actuator bias increased slightly and was kept at a constant level of just above -0.2 V, effectively leaving the RMED in a flat, not deformed state (Figure 6D-II) and preventing possible damage from and to the actuator. Similarly, when a nerve fiber was grasped by the RMED, the target curvature defined by the setpoint could not be reached (Figure 6E), and without the obstacle detection algorithm, the actuator proceeded to compress the nerve with the maximum bias voltage (Figure 6F-I), thus potentially mechanically endangering the nerve fiber. However, when the obstacle detection algorithm was enabled, the compression was stopped shortly after the RMED actuation encountered resistance, the controller did not attempt to fully curl the device, and the nerve fiber was held gently (Figure 6F-II). In a potential application scenario, a soft robotic nerve clamp should mechanically detect tissue for gentle manipulation during neural surgery and hold it in place with as little force as possible, thus preventing surgical injuries.[67–69] We can roughly estimate that the typical handling of a nerve fiber bundle during surgery requires about 0.3 mN (calculation can be found in the Note S1,[70] Supporting Information). Regarding their blocking force of 3.2 mN, RMEDs can easily supply this force, while the application of too much force is prevented through feedback control.

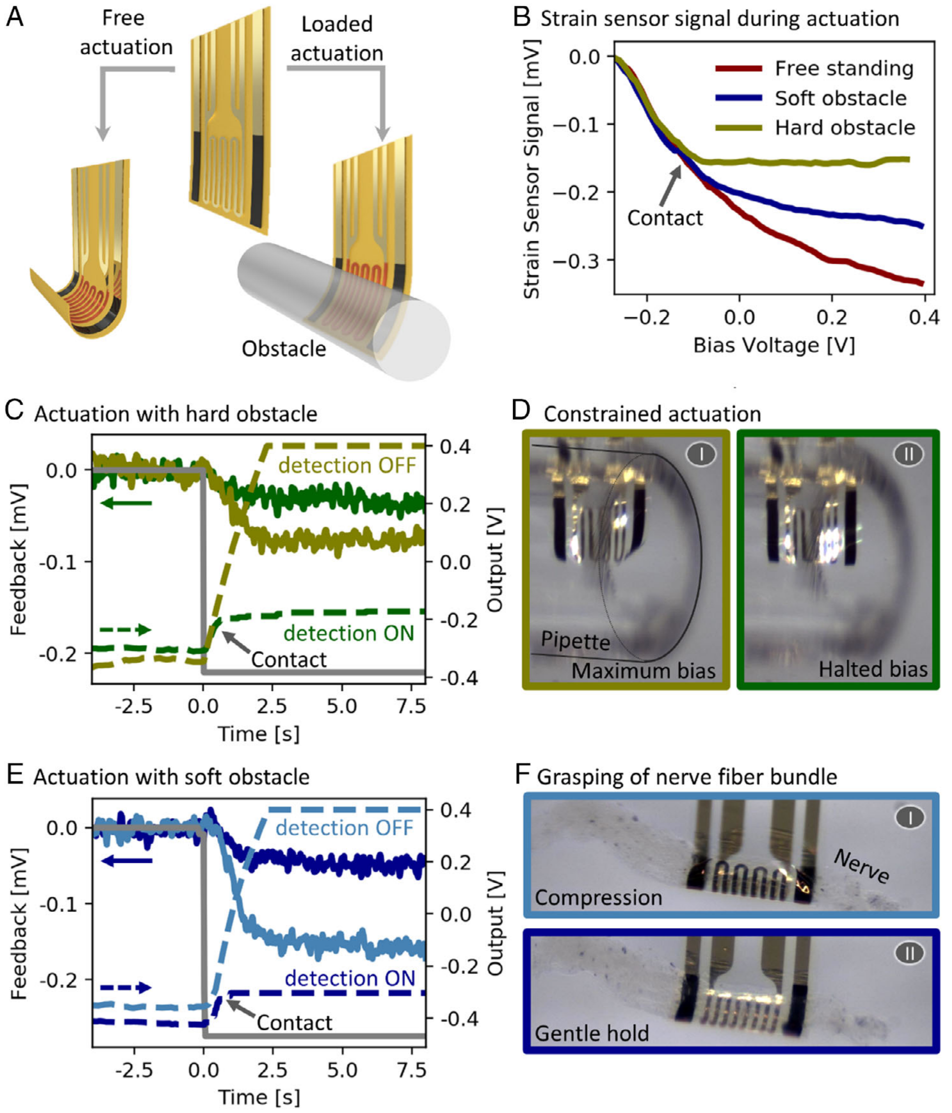

Figure 6. Feedback controlled reshaping of the RMED with various constrains. The width of all RMEDs is 500 µm. A) Schematic of the experiments depicts actuation that is free (left) and constrained by an obstacle (right). B) Graphs displaying strain gauge signals during actuation that is free, constrained with a soft object that can be compressed, or a hard object. Contact with an obstacle is detected when the signal deviates from the reference curve (free actuation). C) Feedback controlled actuation against a hard object. Automatic obstacle detection that holds the actuator bias upon contact is turned off (light green) or on (dark green). D) Corresponding micrographs displaying actuation against a pipette (hard obstacle). E) Grasping a soft object. The nerve is compressed with maximal force when object detection is turned off (light blue) or held gently when turned on (dark blue). F) Corresponding micrographs of grasped nerve fiber.

3. Conclusion

We have realized RMEDs that are capable of feedback-controlled actuation and thereby establish a strong base for a new generation of soft microrobotics. The device fabrication is based on wafer-scale parallel monolithic processes and provides 22 fully integrated devices per wafer. The incorporation of a metal–organic SL enabled the swift and reliable release of the ultrathin structures. The fast and biocompatible electroactive polymer actuators are capable of actively reshaping the device into flat or curved geometries while requiring bias voltages below ±1 V and occupying as little as 20% of the device area. The rest of the polymer carrier area is used for either one of two different types of microelectronic sensors, which monitor the device shape or position. PID control of a fully integrated IEAP actuator–sensor system was successfully demonstrated at the microscale, which represents an important milestone in the decade-old development of microscale soft robotics. The implemented obstacle detection algorithm is crucial for safe operation of the RMED and gentle handling of neural tissue.

The PID control algorithm implemented in this work, which is the simplest and most limited control scheme, was chosen mostly for demonstration purposes. More elaborated and specialized control schemes will be required for intricate real-world applications.

This work contributes to the effort to close the gap between shapeable microelectronics and soft robotics. Although we demonstrated the simplest type of microrobot, one that has one single degree of feedback-driven actuation, the proposed technology leads the path toward interesting applications such as diameter- and force-tunable nerve cuffs or integrated microrobotic catheters.

These future microrobotic systems will demand highly complex shape control, which can only be realized with large sets of independent microactuators. For example, such a robotic system could be a microcatheter composed of an array of actuated hinges and sensors, where the end effector position can be controlled through the pairwise assessment of deflection angles at each joint, down to a known reference position. A key challenge in implementing distributed microactuator systems is the necessity for electrical interconnects for each individual actuator and sensor, a requirement that restricts the number of individual functional components per surface area. This will be resolved through the integration of active electronics such as transistor matrices and shift registers.[2] These digital circuits drastically reduce the amount of required electrical contacts and facilitate a high densities of electronic components.

The presented fabrication strategy enables the integration of conductive polymer actuators and sophisticated microelectronic devices together onto flexible substrates. These processes, however, are based on a purely 2D fabrication scheme and can only result in 2D structures. Complex 3D microrobotic systems, however, will require both, flexible and mechanically stable components. While purely 2D films cannot offer highly stable anchor sites for actuators, robust 3D structures can be created through microscale self-assembly strategies such as rolling, folding, or buckling.[7] These will allow to reshape 2D structures with integrated actuators and advanced electronics to complex 3D microrobotic systems.

4. Experimental Section

Substrates and Materials: Float glasses with dimension of 50×50 mm^2 and a thickness of 1 mm were cleaned and coated with an adhesion layer as previously reported.[53] The metal–organic SL and PI were synthesized following our previously reported procedures.[24,54,55]

Fabrication of Shapeable Polymeric Stacks: To pattern the SL, 1 mL of SL solution was run through a 1 µm glass fiber filter and spin-coated at 3000 rpm for 60 s. The sample was then dried under a constant flow of nitrogen at 35 °C for 10 min and exposed with UV light at 240 mJ cm^{-2} through a glass/Cr mask using a 1000 W SUSS MA6 mask aligner (Karl Suss KG-Gmbh & Co., Munich-Garching, Germany). Samples were then developed for 30 s in deionized (DI) water, dried with a compress nitrogen gun and rinsed in (1-methoxy-2-propyl) acetate to remove excess photo initiator. All chemicals were purchased from Sigma-Aldrich (Sigma-Aldrich Co. LLC, Germany) unless noted otherwise. The sample was hard baked for 10 min at 220 °C. The final layer thickness was around 250 nm. To form the PI carrier, 1 mL of PI solution was spin-coated at 4000 rpm for 60 s and dried under a constant stream of nitrogen for 10 min at 50 °C. Exposure was conducted in a similar fashion to the SL with a total dosage of 500 mJ cm^{-2}. PI structures were developed for 2.5 min in a mixture of *N*-ethyl-pyrillidone (NEP), diethylene-glycol-monoethyl-ether (DEGMEE), and ethanol with a volume ratio of 4:2:1 and successively rinsed with (1-methoxy-2-propyl) acetate for 30 s. After a 10 min hard bake and imidization at 220 °C under a stream of nitrogen, the final layer thickness was around 500 nm. To remove residual PI between the patterned structures, samples were cleaned with oxygen plasma (100 W) for 2 min (Diener Femto). The spin speed was adjusted for both layers to compensate for viscosity variations to ensure constant layer thicknesses.

Fabrication of Magnetic Spin Valve Sensors: SVMSs[53] (long axis: 85 µm, short axis: 55 µm) were patterned on structured PI membranes through a standard lift-off process using a photoresist layer (AZ5214E Microchemicals GmbH, Ulm, Germany). The magnetic stack was deposited by magnetron sputtering (2.4×10^{-6} mbar base pressure, 1.4×10^{-3} mbar Ar atmosphere, 100 W power). Lift-off was conducted in acetone and the magnetic stacks were contacted electrically with Au electrodes (thickness 30 nm). The samples were annealed at 300 °C for 1 h in a constant magnetic field of 1 T to define the sensor magnetization orthogonal or with a 45° tilt to the actuation axis.

Fabrication of Electrodes and Strain Gauges: Au electrodes for PPy actuators, GSSG, and connections for SVMSs were patterned through a standard lift of process. Photoresist AZ5214e was photopatterned and 4/30 nm Ti/Au layers were e-beam evaporated on the sample. Resist and excess Au were removed with acetone. Electrodes and sensors were insulated with a 20 nm layer of Al$_2$O$_3$ which was patterned by wet etching with a 2.7% aqueous solution of tetra-methyl-ammonium-hydroxide (TMAH) for 10 min through a photoresist mask that was subsequently removed with acetone. Areas dedicated for PPy deposition and contacts were cleared from Al$_2$O$_3$.

Deposition of PPy Actuators: To fabricate a pair of PPy actuators, two Au electrodes (width: 50 µm, length: 350 µm) patterned along the edges of a PI carrier platform were first cleaned for 30 s in a 100 W oxygen plasma and connected in a three-electrode electrochemical setup as working electrodes. A AgCl plated Ag wire (Thermo Fischer Scientific) was used as reference electrode and a Au plated Cu rod (3 mm diameter) was used as counter electrode. Electropolymerization of pyrrole was conducted similar to published procedures.[31] Pyrrole monomers were distilled and stored at −20 °C. The monomer solution was prepared by adding 0.278 mL pyrrole in 40 mL of 0.1 M NaDBS aqueous solution, and roll-mixed for 20 min to obtain a homogeneous 0.1 M pyrrole solution. Using a PGU20A potentiostat/galvanostat (IPS), 500 mV versus Ag/AgCl were applied to the samples to polymerize a layer of PPy onto the Au electrodes. The deposition current, initially around 0.1 µA, increased during the first 5 s and stabilized around 4 µA which corresponds to a current density of 10 mA cm^{-2}. The deposition time was adjusted to control the PPy layer thickness. For instance, a deposition charge of 0.13 mA·s after 35 s of deposition yielded a PPy layer thickness of 2.4 µm. No PPy deposition was observed on gold electrodes that were insulated with Al$_2$O$_3$. After deposition, the sample was removed from the monomer bath, rinsed with DI water, and placed in 2% HCl aqueous solution to dissolve the SL. Then, the sample was immersed in a three-electrode electrochemical cell with 0.1 M NaDBS as electrolyte and the actuators were activated with a cycling potential between 0 and −1 V versus Ag/AgCl with a scan speed of 100 mV s^{-1}. Typically, the first cycle would show a significantly higher reduction peak at −900 mV that decreased in magnitude and shifted to −800 mV for successive cycles. Oxidation peaks were found at −500 mV. Initial actuation was observed after three to four cycles. Maximum actuator curvature then increased and stabilized after typically 10 cycles. Actuators were successfully operated in solutions of 0.1 M NaDBS, 0.15 M NaCl, and phosphate-buffered saline (PBS).

Control of Actuators and Sensors: For the simultaneous read out of sensor data and supply of actuator bias voltage, a custom-made PCB equipped with an 8-channel differential 32-bit ADC, and a 16-bit DAC operating at 1 kHz was used. Acquisition, conversion, and display of sensor data, as well as the management of operator inputs, were governed by a custom-written Python program using the PyVisa library and interfaced through a graphical user interface coded in PyQt5. The counter electrode was connected to ground in a two-electrode setup without reference electrode. Actuators were connected to the DAC which supplied voltages of ±10 V versus ground and secured with a 1.2 V safety diode. Sensors were operated in a four-probe mode with a probing current of 1 mA that was supplied by a low dropout (LDO) constant current regulator. The voltage drop across the sensors was low pass noise filtered with an *RC* element ($C = 1\ \mu F$, $R = 1\ k\Omega$) and measured using the onboard ADC. Board communication was governed by the NI Visa driver.

Preparation of Neuronal Tissue: Ex vivo sciatic nerves were taken from nonused sources from running projects of generating mutant and rederiving mouse lines by in-vitro fertilisation (IVF) with frozen sperm in the Transgenic Core Facility of the Max Planck Institute of Molecular Cell Biology and Genetics in Dresden (MPI-CBG). The Transgenic Core Facility holds active permissions and works under the principles of the 3Rs[71] with animals living under specific pathogen free (SPF) conditions. To start the sciatic nerve retrieval, the already dead mouse was placed in a prone position to make an incision in the skin of the dorsal thigh in parallel direction to the femur. With small and sharp scissors, the skin tissue was placed away from the underlying muscle. The muscle was then divided in two sections with a delicate dissection to make the sciatic nerve visible. Then the extremes of the nerve were cut to retrieve the section of interest for further experiments. The sciatic nerve was then further manually separated into nerve fiber bundles of desired diameter. Experiments were conducted under licenses no. DD24.1-5131/394/78 (TVV74/2017) (Permission – Generating mouse models) and DD24.1-5131/461/1 (Permission – Biotechnologies).

Supporting Information

Supporting Information is available from the Wiley Online Library or from the author.

Acknowledgements

The authors thank C. Krien and I. Fiering (Leibniz IFW Dresden) for the deposition of metallic thin films as well as L. Schröder and C. Leger for the help in the clean room and synthesis of materials. The support in the development of the experimental setups from the research technology department of the Leibniz IFW Dresden and the clean room team headed by R. Engelhard (Leibniz IFW Dresden) is greatly appreciated. The authors thank F. Hebenstreit (Leibniz IFW Dresden) for her support in the retrieval of mouse nerve tissues, Dr. Volker Neu for support with AFM measurements, and thank Eric Eisner for his support with the electrical connection of samples. This work is part of the projects that have received funding from the European Research Council (ERC) under the European Union's Horizon 2020 research and innovation program (grant agreement nos. 835268 and 853609). This work was supported by the German Research Foundation DFG (Gottfried Wilhelm Leibniz Prize granted in 2018, SCHM 1298/22-1 and KA5051/1-1) and DFG SPP 1857 ESSENCE grant (KA5051/1-1 and ME4868/2-1).

Correction added on 23 August 2022, after first online publication: Projekt DEAL funding statement has been added.

Open Access funding enabled and organized by Projekt DEAL.

Conflict of Interest

The authors declare no conflict of interest.

Keywords

feedback control, magnetic sensors, microactuators, shapeable electroactive polymers, soft microrobots

Received: October 18, 2020
Revised: December 9, 2020
Published online: January 21, 2021

[1] J. C. Yeo, C. T. Lim, *Microsyst. Nanoeng.* **2016**, *2*, 16043.
[2] M. Kondo, M. Melzer, D. Karnaushenko, T. Uemura, S. Yoshimoto, M. Akiyama, Y. Noda, T. Araki, O. G. Schmidt, T. Sekitani, *Sci. Adv.* **2020**, *6*, 1.
[3] T. Yokota, Y. Inoue, Y. Terakawa, J. Reeder, M. Kaltenbrunner, T. Ware, K. Yang, K. Mabuchi, T. Murakawa, M. Sekino, W. Voit, T. Sekitani, T. Someya, *Proc. Natl. Acad. Sci.* **2015**, *112*, 14533.
[4] Z. Xiang, S. C. Yen, N. Xue, T. Sun, W. M. Tsang, S. Zhang, L. De Liao, N. V. Thakor, C. Lee, *J. Micromech. Microeng.* **2014**, *24*, 65015.
[5] S. P. Lacour, S. Benmerah, E. Tarte, J. Fitzgerald, J. Serra, S. McMahon, J. Fawcett, O. Graudejus, Z. Yu, B. Morrison, *Med. Biol. Eng. Comput.* **2010**, *48*, 945.
[6] M. A. González-González, A. Kanneganti, A. Joshi-Imre, A. G. Hernandez-Reynoso, G. Bendale, R. Modi, M. Ecker, A. Khurram, S. F. Cogan, W. E. Voit, M. I. Romero-Ortega, *Sci. Rep.* **2018**, *8*, 1.
[7] D. Karnaushenko, T. Kang, V. K. Bandari, F. Zhu, O. G. Schmidt, *Adv. Mater.* **2020**, *32*, 1902994.
[8] D. Karnaushenko, N. Münzenrieder, D. D. Karnaushenko, B. Koch, A. K. Meyer, S. Baunack, L. Petti, G. Tröster, D. Makarov, O. G. Schmidt, *Adv. Mater.* **2015**, *27*, 6797.
[9] J. Reeder, M. Kaltenbrunner, T. Ware, D. Arreaga-Salas, A. Avendano-Bolivar, T. Yokota, Y. Inoue, M. Sekino, W. Voit, T. Sekitani, T. Someya, *Adv. Mater.* **2014**, *26*, 4967.
[10] W. Choi, M. Akbarian, V. Rubtsov, C. J. Kim, *IEEE Trans. Ind. Electron.* **2009**, *56*, 1005.
[11] J. Paek, I. Cho, J. Kim, *Sci. Rep.* **2015**, *5*, 1.
[12] S. Li, D. M. Vogt, D. Rus, R. J. Wood, *Proc. Natl. Acad. Sci.* **2017**, *114*, 13132.
[13] G. Kofod, W. Wirges, M. Paajanen, S. Bauer, *Appl. Phys. Lett.* **2007**, *90*, 1.
[14] T. Xu, J. Zhang, M. Salehizadeh, O. Onaizah, E. Diller, *Sci. Robot.* **2019**, *4*, eaav4494.
[15] E. Diller, M. Sitti, *Adv. Funct. Mater.* **2014**, *24*, 4397.
[16] F. Gabler, D. D. Karnaushenko, D. Karnaushenko, O. G. Schmidt, *Nat. Commun.* **2019**, *10*, 3013.
[17] J.-H. Na, A. A. Evans, J. Bae, M. C. Chiappelli, C. D. Santangelo, R. J. Lang, T. C. Hull, R. C. Hayward, *Adv. Mater.* **2015**, *27*, 79.
[18] J. C. Breger, C. Yoon, R. Xiao, H. R. Kwag, M. O. Wang, J. P. Fisher, T. D. Nguyen, D. H. Gracias, *ACS Appl. Mater. Interfaces* **2015**, *7*, 3398.
[19] V. Magdanz, G. Stoychev, L. Ionov, S. Sanchez, O. G. Schmidt, *Angew. Chem. Int. Ed.* **2014**, *53*, 2673.
[20] H. Zeng, O. M. Wani, P. Wasylczyk, R. Kaczmarek, A. Priimagi, *Adv. Mater.* **2017**, *29*, 1701814.
[21] M. Amjadi, M. Sitti, *ACS Nano* **2016**, *10*, 10202.
[22] M. Amjadi, M. Sitti, *Adv. Sci.* **2018**, *5*, 1800239.
[23] T. S. Shim, S. H. Kim, C. J. Heo, H. C. Jeon, S. M. Yang, *Angew. Chem. Int. Ed.* **2012**, *51*, 1420.
[24] D. D. Karnaushenko, D. Karnaushenko, D. Makarov, O. G. Schmidt, *NPG Asia Mater.* **2015**, *7*, e188.
[25] A. Fannir, R. Temmer, G. T. M. Nguyen, L. Cadiergues, E. Laurent, J. D. W. Madden, F. Vidal, C. Plesse, *Adv. Mater. Technol.* **2019**, *4*, 1800519.
[26] S. Ma, Y. Zhang, Y. Liang, L. Ren, W. Tian, L. Ren, *Adv. Funct. Mater.* **2019**, *30*, 1908508.
[27] F. Mashayekhi Mazar, J. G. Martinez, M. Tyagi, M. Alijanianzadeh, A. P. F. Turner, E. W. H. Jager, *Adv. Mater.* **2019**, *31*, 1901677.
[28] H. S. Wang, J. Cho, D. S. Song, J. H. Jang, J. Y. Jho, J. H. Park, *ACS Appl. Mater. Interfaces* **2017**, *9*, 21998.
[29] K. K. Leang, Y. Shan, S. Song, K. J. Kim, *IEEE/ASME Trans. Mechatronics* **2012**, *17*, 345.
[30] E. Smela, N. Gadegaard, *J. Phys. Chem. B* **2001**, *105*, 9395.

[31] E. Smela, O. Inganäs, I. Lundstrom, *Science* **1995**, *268*, 1735.
[32] E. D. Daneshvar, E. Smela, *Adv. Healthcare Mater.* **2014**, *3*, 1026.
[33] C. Immerstrand, E. W. H. Jager, K.-E. Magnusson, T. Sundqvist, I. Lundström, O. Inganäs, K. H. Peterson, *Med. Biol. Eng. Comput.* **2003**, *41*, 357.
[34] E. W. H. Jager, O. Inganäs, I. Lundström, *Science* **2000**, *288*, 2335.
[35] E. W. H. Jager, C. Immerstrand, K. H. Peterson, K. E. Magnusson, I. Lundström, O. Inganäs, *Biomed. Microdevices* **2002**, *4*, 177.
[36] E. W. H. Jager, E. Smela, O. Inganäs, *Science* **2000**, *290*, 1540.
[37] M. Tyagi, J. Pan, E. W. H. Jager, *Microsyst. Nanoeng.* **2019**, *5*, 1.
[38] Y. Zhong, S. Lundemo, E. W. H. Jager, *Smart Mater. Struct.* **2018**, *27*, 74006.
[39] S. W. John, G. Alici, C. D. Cook, *IEEE/ASME Trans. Mechatronics* **2010**, *15*, 149.
[40] D. Melling, S. Wilson, E. W. H. Jager, *Smart Mater. Struct.* **2013**, *22*, 104021.
[41] Y. Liu, Q. Gan, S. Baig, E. Smela, *J. Phys. Chem. C* **2007**, *111*, 11329.
[42] N. Q. Khuyen, Z. Zondaka, M. Harjo, J. Torop, T. Tamm, R. Kiefer, *Polymers* **2019**, *11*, 849.
[43] C. M. Druitt, G. Alici, in *2013 IEEE/ASME Int. Conf. Adv. Intell. Mechatronics Mechatronics Hum. Wellbeing*, Vol. *2013*, IEEE, New York, NY **2013**, p. 373.
[44] J. Schumacher, T. F. Otero, V. H. Pascual, *Electroact. Polym. Actuators Devices* **2017**, *10163*, 1016308.
[45] K. Kruusamäe, A. Punning, A. Aabloo, K. Asaka, *Actuators* **2015**, *4*, 17.
[46] H. Cheng, F. Zhao, J. Xue, G. Shi, L. Jiang, L. Qu, *ACS Nano* **2016**, *10*, 9529.
[47] K. Kruusamäe, P. Brunetto, S. Graziani, A. Punning, G. Di Pasquale, A. Aabloo, *Polym. Int.* **2010**, *59*, 300.
[48] M. Pyo, C. C. Bohn, E. Smela, J. R. Reynolds, A. B. Brennan, *Chem. Mater.* **2003**, *15*, 916.
[49] K. Rohtlaid, L. Seurre, G. T. M. Nguyen, G. Curley, C. Soyer, S. Grondel, F. Vidal, C. Plesse, E. Cattan, *Smart Mater. Struct.* **2020**, *29*, 09LT01.
[50] V. K. Bandari, Y. Nan, D. Karnaushenko, Y. Hong, B. Sun, F. Striggow, D. D. Karnaushenko, C. Becker, M. Faghih, M. Medina-Sánchez, F. Zhu, O. G. Schmidt, *Nat. Electron.* **2020**, *3*, 172.
[51] M. Z. Miskin, A. J. Cortese, K. Dorsey, E. P. Esposito, M. F. Reynolds, Q. Liu, M. Cao, D. A. Muller, P. L. McEuen, I. Cohen, *Nature* **2020**, *584*, 557.
[52] J. T. Reeder, T. Kang, S. Rains, W. Voit, *Adv. Mater.* **2018**, *30*, 1706733.
[53] C. Becker, D. Karnaushenko, T. Kang, D. D. Karnaushenko, M. Faghih, A. Mirhajivarzaneh, O. G. Schmidt, *Sci. Adv.* **2019**, *5*, eaay7459.
[54] D. D. Karnaushenko, D. Karnaushenko, H. Grafe, V. Kataev, B. Büchner, O. G. Schmidt, *Adv. Electron. Mater.* **2018**, *4*, 1800298.
[55] D. Karnaushenko, D. D. Karnaushenko, D. Makarov, S. Baunack, R. Schäfer, O. G. Schmidt, *Adv. Mater.* **2015**, *27*, 6582.
[56] D. Karnaushenko, T. Kang, O. G. Schmidt, *Adv. Mater. Technol.* **2019**, *4*, 1800692.
[57] M. Christophersen, B. Shapiro, E. Smela, *Sens. Actuators B* **2006**, *115*, 596.
[58] P. Du, X. Lin, X. Zhang, *Sens. Actuators A* **2010**, *163*, 240.
[59] J. F. Shackelford, Y.-H. Han, S. Kim, S.-H. Kwon, *CRC Materials Science and Engineering Handbook*, CRC Press, Boca Raton, MA **2016**.
[60] R. Fish, L. Geddes, *J. Plast. Surg.* **2009**, *9*, 407.
[61] E. Smela, M. Kallenbach, J. Holdenried, *J. Microelectromech. Syst.* **1999**, *8*, 373.
[62] D. Bhakta, J. M. Miller, *Indian Pacing Electrophysiol. J.* **2008**, *8*, 32.
[63] S. L. Charreyron, B. Zeydan, B. J. Nelson, in *Proc. – IEEE Int. Conf. Robot. Autom.* IEEE, New York, NY **2017**, p. 4843.
[64] SASB/SCC39 – SCC39 – International Committee on Electromagnetic Safety, *C95.1-2019 – IEEE Standard for Safety Levels with Respect to Human Exposure to Electric, Magnetic, and Electromagnetic Fields, 0 Hz to 300 GHz*, IEEE, New York, NY IEEE **2019**.
[65] K. H. Ang, G. Chong, Y. Li, *IEEE Trans. Control Syst. Technol.* **2005**, *13*, 559.
[66] A. Hunt, Z. Chen, X. Tan, M. Kruusmaa, *Smart Mater. Struct.* **2016**, *25*, 035016.
[67] H. C. Powell, R. R. Myers, *Lab Invest.* **1986**, *55*, 91.
[68] T. Mortimer, W. F. Agnew, K. Horch, P. Citron, G. Creasey, C. Kantor, *IEEE Trans. Rehabil. Eng.* **1995**, *3*, 145.
[69] C. J. De Luca, L. J. Bloom, L. D. Gilmore, *Orthopedics* **1987**, *10*, 777.
[70] Z. Liu, G. Zhang, Q. Jin, Y. Gao, *Neural Regen. Res.* **2010**, *7*, 2299.
[71] P. Flecknell, *ALTEX* **2002**, *19*, 73.